

Observation of dislocation-induced topological modes in a three-dimensional acoustic topological insulator

Haoran Xue,^{1,*} Ding Jia,^{2,*} Yong Ge,² Yi-jun Guan,² Qiang Wang,¹
Shou-qi Yuan,² Hong-xiang Sun,^{2,†} Y. D. Chong,^{1,3,‡} and Baile Zhang^{1,3,§}

¹*Division of Physics and Applied Physics, School of Physical and Mathematical Sciences,
Nanyang Technological University, Singapore 637371, Singapore*

²*Research Center of Fluid Machinery Engineering and Technology,*

School of Physics and Electronic Engineering, Jiangsu University, Zhenjiang 212013, China

³*Centre for Disruptive Photonic Technologies, Nanyang Technological University, Singapore 637371, Singapore*

The interplay between real-space topological lattice defects and the reciprocal-space topology of energy bands can give rise to various novel phenomena, such as one-dimensional topological helical modes bound to screw dislocations in three-dimensional topological insulators. Here, we present a direct experimental observation of this intriguing phenomenon using an acoustic analog of a weak three-dimensional topological insulator. The existence of topological helical modes bound to the dislocation is verified experimentally through spin-resolved field mapping, and numerically through tight-binding and finite-element calculations. The one-dimensional helical channels can serve as robust waveguides in three-dimensional settings. This experiment paves the way to studying the novel physical modes and functionalities enabled by topological lattice defects in three-dimensional classical topological materials.

It has long been known that crystalline materials can host topological defects, which possess nontrivial real-space topological features that protect them from being eliminated by local perturbations [1, 2]. A separate type of topological phenomenon in crystalline materials is band topology, which is generally defined in reciprocal space and leads to the formation of topologically protected boundary modes in real space [3, 4]. When topological lattice defects and nontrivial band topology are simultaneously present, the interplay between them can lead to many interesting phenomena [5–18]. In a paradigmatic example, screw dislocations occurring in three-dimensional (3D) topological insulators (TIs) are predicted to give rise to one-dimensional (1D) topologically-protected helical modes [5]; the number of induced topological modes is determined by the Burgers vector \mathbf{B} of the dislocation and a reciprocal vector $\mathbf{G}_{\mathbf{v}}$ defined by the three weak topological indices [19] through a bulk-dislocation correspondence $\mathbf{B} \cdot \mathbf{G}_{\mathbf{v}}/2\pi$ [5]. This and related phenomena have been theoretically studied in the context of strong/weak 3D electronic TIs [5–7, 11], 3D photonic Chern crystals [20], and weak 3D photonic TIs in synthetic dimensions [21]. On the experimental front, signatures of dislocation-induced topological modes in real materials have been seen in a very limited number of experiments [22, 23], based on conductivity measurements [22] or probes of the local density of states [23]. Direct observations of dislocation-induced topological modes, including their crucial helical features, remain lacking. On the other hand, artificial structures such as photonic crystals and acoustic crystals provide high levels of controllability and flexibility in design, fabrication and characterization; they have been used to demonstrate some interesting aspects of the interplay between topological lattice defects in topological materials, such

as bound states bound to dislocations in photonic Chern insulators [24] and weak 2D magnetomechanical TI [25], disclination waveguiding in valley photonic crystals [16], and fractional defect states in 2D crystalline TIs [26, 27].

Topological modes bound to topological lattice defects in artificial materials have interesting properties that may be useful for practical applications. Dislocation-induced topological helical channels in 3D TIs, for instance, can serve as robust 1D waveguides. Compared to other topological waveguide designs such as hinge modes in 3D higher-order TIs [28–30], they have the advantages of larger bandwidth (hinge modes usually exist inside a surface gap while dislocation-induced modes span the whole bulk gap), and the ability to support multimode transport (by increasing the Burgers vector or the spin Chern number).

In this Letter, we present a direct experimental observation of dislocation-induced topological helical modes in a 3D acoustic TI. The sample consists of stacked 2D acoustic TIs with vanishing interlayer coupling, implementing a weak 3D acoustic TI with $\mathbf{G}_{\mathbf{v}} = (0, 0, 1)\frac{2\pi}{a_z}$. A screw dislocation with $\mathbf{B} = (0, 0, a_z)$ is fabricated into the center of the sample. With this setup, we obtain a pair of gapless helical modes inside the topological bandgap, as predicted by the bulk-dislocation correspondence [5]. The existence of the helical modes is determined experimentally from field-mapping measurements, corroborated by tight-binding calculations and full-wave simulations. The experimental observations are obtained by mapping out spin-resolved distributions of the dislocation-induced helical modes over the entire sample (both on the surface and inside the bulk).

Our design process is schematically illustrated in Fig. 1. We start with a 2D TI that hosts a pair of topologically-protected helical modes on its edges

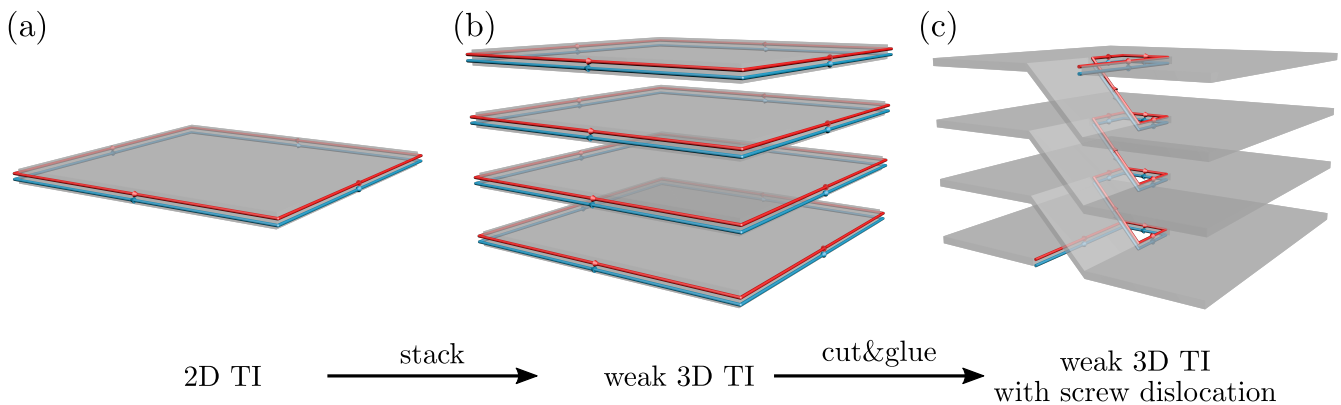


FIG. 1. Construction of a 3D weak TI with a screw dislocation. (a) The starting point is a 2D TI with helical edge modes. (b) To construct a weak 3D TI, the 2D TIs are stacked along z . In the limit of zero inter-layer couplings, the surface modes of the weak 3D TI are nothing but the helical edge modes of the decoupled 2D layers. (c) A screw dislocation is introduced by a cut-and-glue procedure; the helical edge modes on the bottom and top layers connect to modes running along the dislocation.

[31, 32], as shown in Fig. 1(a). A weak 3D TI can then be constructed by stacking the 2D TIs along z direction. The bulk bandgap is maximized by letting the couplings between adjacent layers vanish. With this setup, the gapless surface states on the side surfaces of this weak 3D TI are intrinsically 2D: they propagate only in the xy plane of each decoupled layer (Fig. 1(b)). A screw dislocation along z is then introduced by the “cut and glue” procedure shown in Fig. 1(c). In tight-binding models as well as the real experimental sample, this can be accomplished by modifying the couplings between certain sites near the center of each layer. Once the dislocation is introduced, there should evidently be a pair of dislocation-induced helical modes, which are connected to the helical edge modes on the bottom and top layers, as shown in Fig. 1(c).

To design the structure, we begin with a tight-binding model for a 2D TI described by a Hamiltonian of the form

$$H = \begin{bmatrix} H_{\uparrow}(\phi) & 0 \\ 0 & H_{\downarrow}(\phi) \end{bmatrix}, \quad (1)$$

where the submatrices $H_{\uparrow,\downarrow}$ describe 2D Chern insulators consisting of square lattices with complex couplings, as depicted in Fig. 2(a). Each is a copy of the Hofstadter model [33], with magnetic flux $\phi = \pm\pi/2$ (thus $H_{\downarrow} = H_{\uparrow}^*$). [34, 35]. The design can be further simplified through the transformation $[\psi_A, \psi_B]^T = u^{-1}[\psi_{\uparrow}, \psi_{\downarrow}]^T$ where [36, 37]

$$u = \begin{bmatrix} 1 & i \\ 1 & -i \end{bmatrix} / \sqrt{2}. \quad (2)$$

Under this transformation, the original complex couplings are replaced by real couplings with either positive or negative sign, as shown in Fig. 2(b). A lattice of this sort can be realized in acoustics using acoustic resonators coupled by properly-designed channels [38].

Fig. 2(c) shows the spectrum of the resulting 2D TI, with open boundary condition along x and periodic boundary condition along y . There are two nontrivial bandgaps traversed by helical edge modes, whose mode profiles are shown in Fig. 2(e). Finally, following the procedure depicted in Fig. 1, we stack the 2D TI to form a weak 3D TI, and introduce a central screw dislocation. Specifically, the dislocation is implemented by replacing the intra-layer couplings along each line segment $x = 0, y > 0$ (where $(x, y) = (0, 0)$ denotes the center of the lattice) with appropriate inter-layer couplings.

Fig. 2(d) shows the calculated spectrum for a lattice of size 16×16 , with periodic boundary conditions imposed along x and y directions to remove the surface modes on the sides. With this simulation geometry, there is an extra dislocation at $(8, 0)$ in addition to the dislocation at $(0, 0)$. In the plot, dislocation-induced helical modes can clearly be seen within the bulk bandgap. Each dispersion curve of dislocation modes is two-fold degenerate, corresponding to the two modes at the two dislocations; red (blue) denote spin \uparrow (\downarrow) for the modes evaluated at $(0, 0)$. The mode profiles are shown in Fig. 2(f).

We now introduce an acoustic lattice that realizes the lattice model described above. It consists of two types of building blocks: acoustic resonators and coupling tubes; similar designs have previously been used to create acoustic realizations of other tight-binding models [38–43]. A photograph of a one-layer sample (without a dislocation) is shown in Fig. 3(a), and a schematic of part it is shown in Fig. 3(b). Each cuboid resonator supports a dipolar mode at around 2144 Hz, and is connected to its neighbors through a series of coupling tubes. The coupling tubes shown in red (blue) in Fig. 3(b) correspond to positive (negative) couplings. Detailed structure parameters of the acoustic lattice are given in the Supplemental Materials [44].

Prior to dealing with the full 3D lattice, we first verify

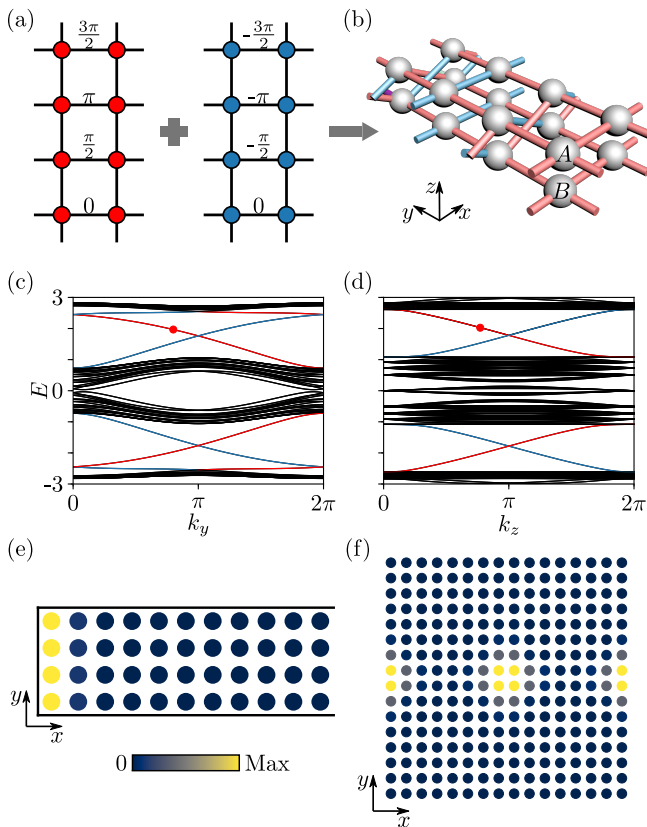


FIG. 2. Lattice model design. (a) Square lattices with magnetic flux $\phi = \pi/2$ (left) and $\phi = -\pi/2$ (right) per plaquette. (b) A lattice model for a 2D TI by combining and transforming the two lattice models in (a). Here, all couplings are real and have the same amplitude. Red and blue colors denote positive and negative couplings, respectively. (c) Edge spectrum for the lattice shown in (b). In the calculation, we use periodic boundary condition for y and open boundary condition for x . Black curves correspond to bulk bands and red/blue curves denote spin up/down modes on the left edge. (d) Dislocation spectrum for a weak 3D TI built up by stacking the 2D TI in (b) with vanishing inter-layer couplings. In the calculation, we take a lattice of size 16×16 and use periodic boundary conditions for both x and y directions. The couplings at $x = 0$ and $y > 0$ are all replaced by inter-layer couplings. This setting leads to two dislocations at $(0,0)$ and $(8,0)$. (e) Profile of the edge mode marked by the red circle in (c). (f) Profile of the dislocation mode marked by the red circle in (d).

the features of the 2D lattice using simulations and experiments. We consider a finite acoustic lattice of size 8×8 (Fig. 3(a)). The simulated eigenfrequencies are plotted in Fig. 3(c), with the frequency windows corresponding to the two bulk bandgaps shaded in grey. The modes inside the bandgaps are indeed edge modes, as can be seen from the eigenmode profile plotted in Fig. 3(d). Throughout this work, we will focus on the second bandgap at ~ 2200 Hz, which is larger.

To verify the existence of the edge modes experimentally, we put a speaker at the left edge (yellow star in

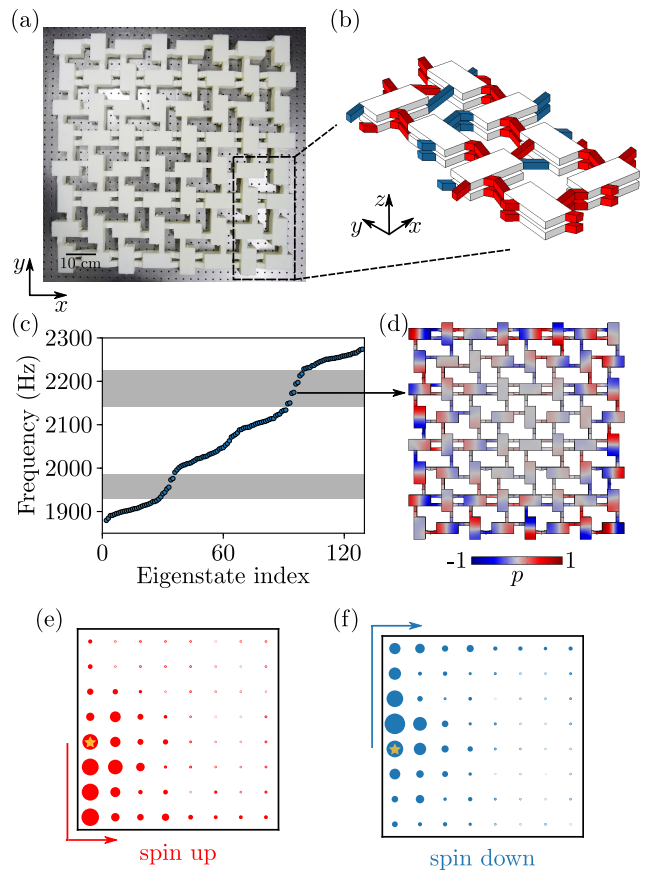


FIG. 3. Design and demonstration of a 2D acoustic TI. (a) Photo of the fabricated sample for the 2D acoustic TI. (b) Unit cell for the acoustic lattice. Here, coupling tubes colored in red/blue enable positive/negative couplings. (c) Simulated eigenfrequencies for the acoustic lattice shown in (a). The shaded grey regions denote the bulk bandgap. (d) Eigenmode profile for one of the in-gap edge modes. (e) and (f) Measured field distributions at 2165 Hz for spin up mode (e) and spin down mode (f).

Figs. 3(e) and 3(f) and measure the acoustic field (both amplitude and phase) in each resonator. Details of the experimental procedure are given in the Supplemental Materials [44]. The spin-resolved fields are obtained as $[\psi_{\uparrow}, \psi_{\downarrow}]^T = u[\psi_A, \psi_B]^T$. Figs. 3(e) and 3(f) show the measured intensity distributions at 2165 Hz for spin up and spin down, respectively. Evidently, the two fields counter-propagate along the edge, as expected of spin-polarized helical edge modes.

Building on this 2D acoustic TI design, we construct a weak 3D acoustic TI with a screw dislocation according to the procedure in Fig. 1. The fabricated sample is shown in Fig. 4(a). It consists of four layers of the 2D acoustic TI with a central screw dislocation, with Burgers vector $\mathbf{B} = (0, 0, a_z)$. A close-up view of the dislocation is shown in Fig. 4(d). Fig. 4(b) shows the simulated dispersion for the 3D acoustic structure, which agrees well with the dispersion obtained using the tight-binding

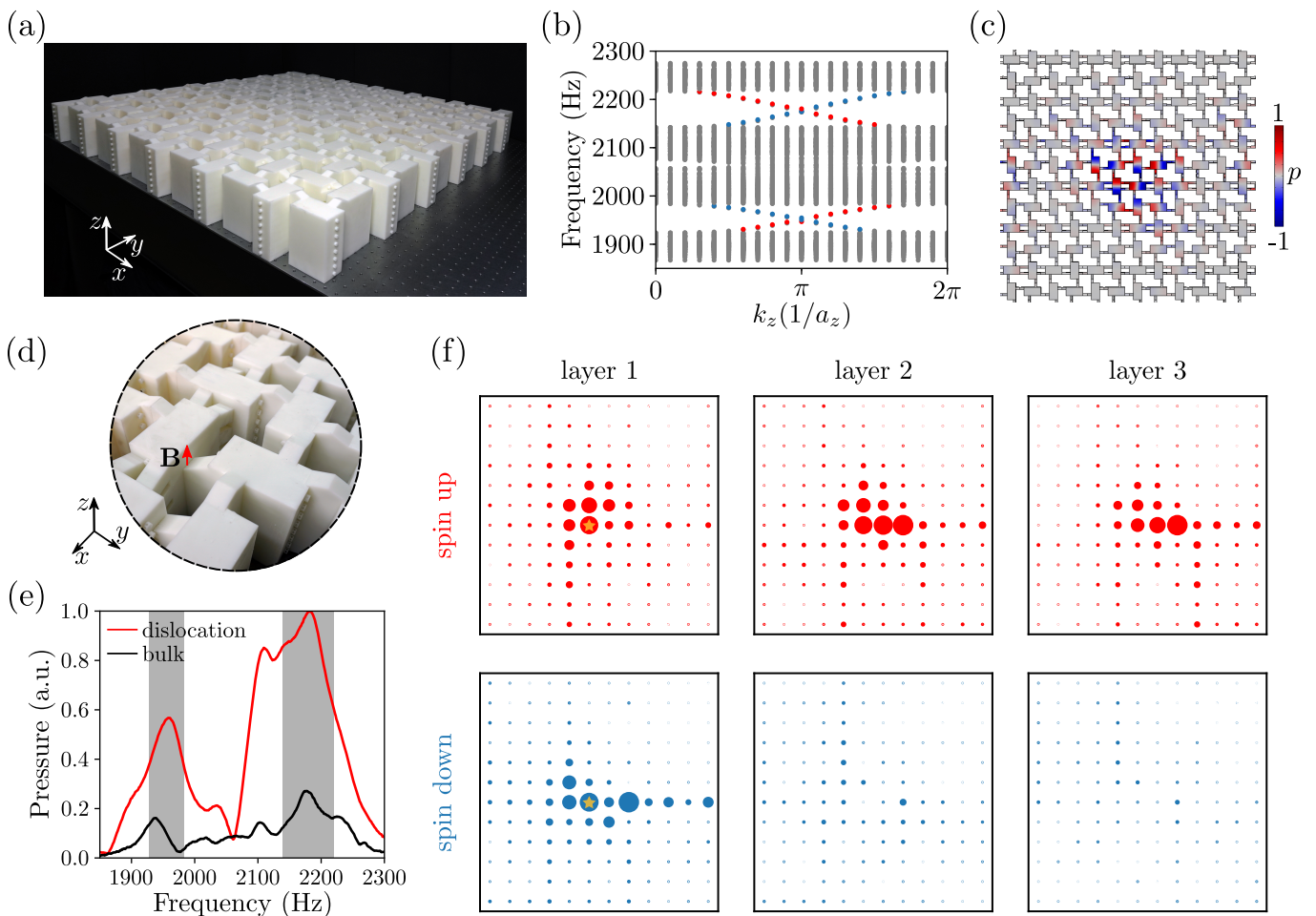


FIG. 4. Observation of dislocation-induced topological helical modes. (a) Photo of the fabricated sample for the weak 3D acoustic TI with dislocation. (b) Simulated bandstructure for the lattice shown in (a). Here, grey dots correspond to bulk modes and red/blue dots represent spin up/spin down dislocation modes. (c) Eigenmode profile for one of the dislocation modes. (d) A zoomed-in photo of sample center area. The Burgers vector \mathbf{B} is denoted by the red arrow. (e) Measured acoustic pressure spectra when the excitation is at the center of the first layer and the detection is at the second layer. Red and black curves are results obtained at one resonator next to the center and away from the center, respectively. (f) Measured acoustic intensity distributions at 2165 Hz in the three layers counted from the top layer. Red and blue colors represent spin up and spin down states, respectively. The subplots within the same column (i.e., the same layer) are normalized by the same value, while the subplots in different columns are normalized by different values.

model (Fig. 2(d)). In particular, we can clearly see the emergence of the dislocation-induced helical modes, with a typical mode profile shown in Fig. 4(c).

To probe the dislocation-induced helical modes experimentally, we inject sound into one of the resonators at the center of the top layer; the source position is indicated by a yellow star in Fig. 4(f). We then scan the acoustic fields inside the whole sample [44]. Fig. 4(e) plots the acoustic pressure spectra measured at two different resonators on the second layer (here the second layer refers to the layer right below the top layer). The red curve comes from measurements taken at a resonator next to the dislocation, which has strong peaks at frequencies corresponding to the predicted bulk bandgaps, where the dislocation modes are expected to occur. The

black curve is derived from measurements taken at a resonator that is $2\sqrt{2}a$ away from the dislocation (a is the spacing between adjacent resonators), and has less pronounced peaks at those frequencies. This indicates that the in-gap modes are localized around the dislocation.

Fig. 4(f) shows site- and spin-resolved acoustic intensity distributions measured at 2165 Hz. As can be seen, the distributions for the two spins are very different. For spin up (upper row), the measured intensity is always localized around the center. For spin down (lower row), however, the intensities in the second the third layers are negligible. This indicates that only spin up states can propagate downwards along the dislocation; in other words, the direction of propagation along the dislocation is locked to the spin. The observed spatial profile and

helical characteristics of the dislocation-induced topological modes agree well with the simulation results shown in Fig. 4(b).

To sum up, we have designed and demonstrated a weak 3D acoustic TI with a screw lattice dislocation. The existence of topological helical modes bound to the dislocation is verified both numerically and experimentally. These 1D dislocation-induced helical channels have the potential to serve as robust waveguides in 3D systems. Our results, together with other recent experimental efforts [17, 45], pave the way to discovering novel phenomena and applications associated with the interaction of nontrivial band topology and topological lattice defects in 3D artificial structures. There are many possibilities for future work, including extending the current design beyond the tight-binding model to achieve a larger bandgap, lower loss and multimode behavior, perhaps by following the ideas in Ref. [20] but with a non-magnetic design. Moreover, the introduction of non-Hermiticity, which is available and can be tuned in various classical topological systems [46–54], may lead to new physical effects yet to be explored [55].

H.X., Q.W., Y.C. and B.Z. acknowledge support from Singapore Ministry of Education Academic Research Fund under Grants No. MOE2016-T3-1-006 and MOE2019-T2-2-085. D.J., Y.G., Y.G., S.Y. and H.S. acknowledge support from the National Natural Science Foundation of China under Grants No. 11774137 and 51779107, the China Postdoctoral Science Foundation under Grant No. 2020M671351, and the State Key Laboratory of Acoustics, Chinese Academy of Science under Grant No. SKLA202115.

* These authors contribute equally.

† jsdxshx@ujs.edu.cn

‡ yidong@ntu.edu.sg

§ blzhang@ntu.edu.sg

- [1] N. D. Mermin, The topological theory of defects in ordered media, *Rev. Mod. Phys.* **51**, 591 (1979).
- [2] J. M. Kosterlitz, Nobel lecture: Topological defects and phase transitions, *Rev. Mod. Phys.* **89**, 040501 (2017).
- [3] M. Z. Hasan and C. L. Kane, Colloquium: topological insulators, *Rev. Mod. Phys.* **82**, 3045 (2010).
- [4] X.-L. Qi and S.-C. Zhang, Topological insulators and superconductors, *Rev. Mod. Phys.* **83**, 1057 (2011).
- [5] Y. Ran, Y. Zhang, and A. Vishwanath, One-dimensional topologically protected modes in topological insulators with lattice dislocations, *Nat. Phys.* **5**, 298 (2009).
- [6] J. C. Teo and C. L. Kane, Topological defects and gapless modes in insulators and superconductors, *Phys. Rev. B* **82**, 115120 (2010).
- [7] K.-I. Imura, Y. Takane, and A. Tanaka, Weak topological insulator with protected gapless helical states, *Phys. Rev. B* **84**, 035443 (2011).
- [8] V. Juričić, A. Mesaros, R.-J. Slager, and J. Zaanen, Universal probes of two-dimensional topological insulators: dislocation and π flux, *Phys. Rev. Lett.* **108**, 106403 (2012).
- [9] A. Rüegg and C. Lin, Bound states of conical singularities in graphene-based topological insulators, *Phys. Rev. Lett.* **110**, 046401 (2013).
- [10] K. Shiozaki and M. Sato, Topology of crystalline insulators and superconductors, *Phys. Rev. B* **90**, 165114 (2014).
- [11] R.-J. Slager, A. Mesaros, V. Juričić, and J. Zaanen, Interplay between electronic topology and crystal symmetry: Dislocation-line modes in topological band insulators, *Phys. Rev. B* **90**, 241403 (2014).
- [12] H. Sumiyoshi and S. Fujimoto, Torsional chiral magnetic effect in a Weyl semimetal with a topological defect, *Phys. Rev. Lett.* **116**, 166601 (2016).
- [13] J. Liu and L. Balents, Anomalous Hall effect and topological defects in antiferromagnetic Weyl semimetals: $\text{Mn}_3\text{Sn}/\text{Ge}$, *Phys. Rev. Lett.* **119**, 087202 (2017).
- [14] R. Queiroz, I. C. Fulga, N. Avraham, H. Beidenkopf, and J. Cano, Partial lattice defects in higher-order topological insulators, *Phys. Rev. Lett.* **123**, 266802 (2019).
- [15] R.-J. Slager, The translational side of topological band insulators, *J. Phys. Chem. Solids* **128**, 24 (2019).
- [16] Q. Wang, H. Xue, B. Zhang, and Y. Chong, Observation of protected photonic edge states induced by real-space topological lattice defects, *Phys. Rev. Lett.* **124**, 243602 (2020).
- [17] Q. Wang, Y. Ge, H.-x. Sun, H. Xue, D. Jia, Y.-j. Guan, S.-q. Yuan, B. Zhang, and Y. Chong, Vortex higher-order Fermi arc induced by topological lattice defects, [arXiv: 2012.08140](https://arxiv.org/abs/2012.08140) (2020).
- [18] T. Li, P. Zhu, W. A. Benalcazar, and T. L. Hughes, Fractional disclination charge in two-dimensional C_n -symmetric topological crystalline insulators, *Phys. Rev. B* **101**, 115115 (2020).
- [19] L. Fu, C. L. Kane, and E. J. Mele, Topological insulators in three dimensions, *Phys. Rev. Lett.* **98**, 106803 (2007).
- [20] L. Lu, H. Gao, and Z. Wang, Topological one-way fiber of second Chern number, *Nat. Commun.* **9**, 5384 (2018).
- [21] Q. Lin, X.-Q. Sun, M. Xiao, S.-C. Zhang, and S. Fan, A three-dimensional photonic topological insulator using a two-dimensional ring resonator lattice with a synthetic frequency dimension, *Sci. Adv.* **4**, eaat2774 (2018).
- [22] H. Hamasaki, Y. Tokumoto, and K. Edagawa, Dislocation conduction in Bi-Sb topological insulators, *Appl. Phys. Lett.* **110**, 092105 (2017).
- [23] A. K. Nayak, J. Reiner, R. Queiroz, H. Fu, C. Shekhar, B. Yan, C. Felser, N. Avraham, and H. Beidenkopf, Resolving the topological classification of bismuth with topological defects, *Sci. Adv.* **5**, eaax6996 (2019).
- [24] F.-F. Li, H.-X. Wang, Z. Xiong, Q. Lou, P. Chen, R.-X. Wu, Y. Poo, J.-H. Jiang, and S. John, Topological light-trapping on a dislocation, *Nat. Commun.* **9**, 2462 (2018).
- [25] I. H. Grinberg, M. Lin, W. A. Benalcazar, T. L. Hughes, and G. Bahl, Trapped state at a dislocation in a weak magnetomechanical topological insulator, *Phys. Rev. Appl.* **14**, 064042 (2020).
- [26] C. W. Peterson, T. Li, W. Jiang, T. L. Hughes, and G. Bahl, Trapped fractional charges at bulk defects in topological insulators, *Nature* **589**, 376 (2021).
- [27] Y. Liu, S. Leung, F.-F. Li, Z.-K. Lin, X. Tao, Y. Poo, and J.-H. Jiang, Bulk–disclination correspondence in topological crystalline insulators, *Nature* **589**, 381 (2021).

- [28] F. Schindler, A. M. Cook, M. G. Vergniory, Z. Wang, S. S. Parkin, B. A. Bernevig, and T. Neupert, Higher-order topological insulators, *Sci. Adv.* **4**, eaat0346 (2018).
- [29] J. Langbehn, Y. Peng, L. Trifunovic, F. von Oppen, and P. W. Brouwer, Reflection-symmetric second-order topological insulators and superconductors, *Phys. Rev. Lett.* **119**, 246401 (2017).
- [30] Z. Song, Z. Fang, and C. Fang, (d- 2)-dimensional edge states of rotation symmetry protected topological states, *Phys. Rev. Lett.* **119**, 246402 (2017).
- [31] C. L. Kane and E. J. Mele, Quantum spin Hall effect in graphene, *Phys. Rev. Lett.* **95**, 226801 (2005).
- [32] B. A. Bernevig, T. L. Hughes, and S.-C. Zhang, Quantum spin Hall effect and topological phase transition in HgTe quantum wells, *Science* **314**, 1757 (2006).
- [33] D. R. Hofstadter, Energy levels and wave functions of Bloch electrons in rational and irrational magnetic fields, *Phys. Rev. B* **14**, 2239 (1976).
- [34] M. Hafezi, E. A. Demler, M. D. Lukin, and J. M. Taylor, Robust optical delay lines with topological protection, *Nat. Phys.* **7**, 907 (2011).
- [35] M. Hafezi, S. Mittal, J. Fan, A. Migdall, and J. Taylor, Imaging topological edge states in silicon photonics, *Nat. Photon.* **7**, 1001 (2013).
- [36] R. Süsstrunk and S. D. Huber, Observation of phononic helical edge states in a mechanical topological insulator, *Science* **349**, 47 (2015).
- [37] J. Ningyuan, C. Owens, A. Sommer, D. Schuster, and J. Simon, Time-and site-resolved dynamics in a topological circuit, *Phys. Rev. X* **5**, 021031 (2015).
- [38] H. Xue, Y. Ge, H.-X. Sun, Q. Wang, D. Jia, Y.-J. Guan, S.-Q. Yuan, Y. Chong, and B. Zhang, Observation of an acoustic octupole topological insulator, *Nat. Commun.* **11**, 2442 (2020).
- [39] M. Xiao, W.-J. Chen, W.-Y. He, and C. T. Chan, Synthetic gauge flux and Weyl points in acoustic systems, *Nat. Phys.* **11**, 920 (2015).
- [40] Y.-X. Xiao, G. Ma, Z.-Q. Zhang, and C. T. Chan, Topological subspace-induced bound state in the continuum, *Phys. Rev. Lett.* **118**, 166803 (2017).
- [41] H. Xue, Y. Yang, F. Gao, Y. Chong, and B. Zhang, Acoustic higher-order topological insulator on a kagome lattice, *Nat. Mater.* **18**, 108 (2019).
- [42] X. Ni, M. Weiner, A. Alu, and A. B. Khanikaev, Observation of higher-order topological acoustic states protected by generalized chiral symmetry, *Nat. Mater.* **18**, 113 (2019).
- [43] H. Xue, Y. Yang, G. Liu, F. Gao, Y. Chong, and B. Zhang, Realization of an acoustic third-order topological insulator, *Phys. Rev. Lett.* **122**, 244301 (2019).
- [44] See online Supplemental Materials.
- [45] L. Ye, C. Qiu, M. Xiao, T. Li, J. Du, M. Ke, and Z. Liu, Topological dislocation modes in three-dimensional acoustic topological insulators, *arXiv: 2104.04172* (2021).
- [46] C. Poli, M. Bellec, U. Kuhl, F. Mortessagne, and H. Schomerus, Selective enhancement of topologically induced interface states in a dielectric resonator chain, *Nat. Commun.* **6**, 6710 (2015).
- [47] S. Weimann, M. Kremer, Y. Plotnik, Y. Lumer, S. Nolte, K. G. Makris, M. Segev, M. C. Rechtsman, and A. Szameit, Topologically protected bound states in photonic parity–time-symmetric crystals, *Nat. Mater.* **16**, 433 (2017).
- [48] S. Weidemann, M. Kremer, T. Helbig, T. Hofmann, A. Stegmaier, M. Greiter, R. Thomale, and A. Szameit, Topological funneling of light, *Science* **368**, 311 (2020).
- [49] H. Zhao, X. Qiao, T. Wu, B. Midya, S. Longhi, and L. Feng, Non-Hermitian topological light steering, *Science* **365**, 1163 (2019).
- [50] W. Zhu, X. Fang, D. Li, Y. Sun, Y. Li, Y. Jing, and H. Chen, Simultaneous observation of a topological edge state and exceptional point in an open and non-Hermitian acoustic system, *Phys. Rev. Lett.* **121**, 124501 (2018).
- [51] H. Gao, H. Xue, Q. Wang, Z. Gu, T. Liu, J. Zhu, and B. Zhang, Observation of topological edge states induced solely by non-Hermiticity in an acoustic crystal, *Physical Review B* **101**, 180303 (2020).
- [52] H. Gao, H. Xue, Z. Gu, T. Liu, J. Zhu, and B. Zhang, Non-Hermitian route to higher-order topology in an acoustic crystal, *Nat. Commun.* **12**, 1888 (2021).
- [53] T. Helbig, T. Hofmann, S. Imhof, M. Abdelghany, T. Kiessling, L. Molenkamp, C. Lee, A. Szameit, M. Greiter, and R. Thomale, Generalized bulk–boundary correspondence in non-Hermitian topoelectrical circuits, *Nat. Phys.* **16**, 747 (2020).
- [54] S. Liu, S. Ma, C. Yang, L. Zhang, W. Gao, Y. J. Xiang, T. J. Cui, and S. Zhang, Gain-and loss-induced topological insulating phase in a non-Hermitian electrical circuit, *Phys. Rev. Appl.* **13**, 014047 (2020).
- [55] X.-Q. Sun, P. Zhu, and T. L. Hughes, Geometric response and disclination-induced skin effects in non-Hermitian systems, *arXiv: 2102.05667* (2021).